

Combined Effects of Anion Substitution and Nanoconfinement on the Ionic Conductivity of Li-Based Complex Hydrides

Roman Zettl, Laura de Kort, Maria Gombotz, H. Martin R. Wilkening, Petra E. de Jongh,* and Peter Ngene*

Cite This: *J. Phys. Chem. C* 2020, 124, 2806–2816

Read Online

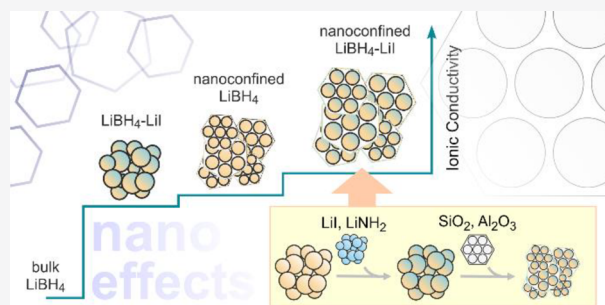
ACCESS |

Metrics & More

Article Recommendations

Supporting Information

ABSTRACT: Solid-state electrolytes are crucial for the realization of safe and high capacity all-solid-state batteries. Lithium-containing complex hydrides represent a promising class of solid-state electrolytes, but they exhibit low ionic conductivities at room temperature. Ion substitution and nanoconfinement are the main strategies to overcome this challenge. Here, we report on the synthesis of nanoconfined anion-substituted complex hydrides in which the two strategies are effectively combined to achieve a profound increase in the ionic conductivities at ambient temperature. We show that the nanoconfinement of anion substituted LiBH_4 ($\text{LiBH}_4\text{--LiI}$ and $\text{LiBH}_4\text{--LiNH}_2$) leads to an enhancement of the room temperature conductivity by a factor of 4 to 10 compared to nanoconfined LiBH_4 and nonconfined $\text{LiBH}_4\text{--LiI}$ and $\text{LiBH}_4\text{--LiNH}_2$, concomitant with a lowered activation energy of 0.44 eV for Li-ion transport. Our work demonstrates that a combination of partial ion substitution and nanoconfinement is an effective strategy to boost the ionic conductivity of complex hydrides. The strategy could be applicable to other classes of solid-state electrolytes.



1. INTRODUCTION

Solid-state electrolytes are indispensable for the realization of safe batteries offering high energy densities^{1,2} crucial for the development of both mobile applications and large-scale stationary systems that can effectively store electricity from renewable but intermittent energy sources such as solar, wind, or tidal. Current battery systems, especially those designed for electric vehicles, may suffer from flammable and volatile organic based liquid electrolytes. In many cases, this narrow electrochemical stability window of conventional aprotic electrolytes prevents the use of anode materials providing high energy densities like metallic lithium. These disadvantages have led to a renewed interest in inorganic solid-state electrolytes, because they are potentially safer than liquid electrolytes and chemically compatible with Li metal. In addition, if sulfur-based cathode materials are considered, they prevent the dissolution and shuttling of polysulfides, which is one of the most serious hurdles that needs to be overcome in these type of batteries that promise high energy densities.³

Various classes of materials have been investigated as solid-state ion conductors for all-solid-state batteries.^{4–8} These materials include garnets,⁹ perovskites,¹⁰ and polymers¹¹ as well as glass type electrolytes.¹² The complex metal hydrides, particularly those containing Li and Na, such as LiBH_4 , $\text{Li}_2\text{B}_{12}\text{H}_{10}$, $\text{NaB}_{10}\text{H}_{10}$, and $\text{NaCB}_{11}\text{H}_{12}$ constitute a relatively new class of solid electrolytes.^{13–17} Due to their lightweight and high hydrogen content, these materials have been

intensively investigated over the last 20 years for reversible hydrogen storage. The hydrogen could be used for fuel cells with polymer electrolyte membranes.^{18–21} Over a decade ago, it was shown that they also exhibit fast ionic conductivity and some also show good electrochemical stability windows up to 3 V versus Li/Li^+ .^{22–24}

The main challenge for solid-state electrolytes in general has been the inherently low room temperature ionic conductivity, compared to liquid electrolytes. Therefore, most research effort has been focused on enhancing the ionic conductivities by structural modifications. For instance, the high ionic conductivity in complex hydrides is often a result of structural phase transition at high temperatures. A typical example is LiBH_4 , which exhibits an ionic conductivity of $1 \times 10^{-3} \text{ S cm}^{-1}$ above 110 °C,^{14,23} due to the formation of the hexagonal phase, whereas at room temperature, the compound crystallizes into the orthorhombic structure, which shows poor ion conductivity.^{25–27}

Two main approaches, which have separately been introduced in literature, have proved to be successful in boosting the room temperature ionic conductivity of solid

Received: November 12, 2019

Revised: January 14, 2020

Published: January 21, 2020

electrolytes, especially complex hydrides. The first approach takes advantage of the partial substitution of the complex anion (e.g., BH_4^- in LiBH_4) by halides such as Cl^- and I^- or by amides.^{28–30} Iso- or aliovalent replacement of the Li^+ cations by Na^+ , Ca^{2+} or Ce^{3+} has been reported as well.^{31–33} Partial ion substitution is generally achieved by high-energy ball milling³⁴ or by heating a physical mixture of the compounds at temperatures of 200 to 300 °C; note that the melting point of LiBH_4 is 278 °C.³⁵ For instance, solid solutions of $\text{LiBH}_4\text{--LiX}$ ($\text{X} = \text{Cl}, \text{Br}, \text{I}$) and $\text{LiBH}_4\text{--Li}_3\text{N}$ or new compounds like in $\text{LiBH}_4\text{--LiNH}_2$ with room temperature ionic conductivities that are much higher than the individual compounds have been reported. Several studies have been conducted to investigate the effect of heat treatment,³⁶ the influence of LiX contents,³⁵ and the influence of the kind of the substituting anion.³⁷

It is generally believed that anion substitution leads to an increase in distance between neighboring BH_4^- units which is associated with weaker Coulomb interactions in LiBH_4 and hence a decrease of the transition temperature at which the compound changes from orthorhombic to hexagonal symmetry.³⁸ Indeed, substitution with larger halide anions leads to stabilization of the hexagonal phase of LiBH_4 at near ambient temperatures as clearly seen in the most investigated anion substituted complex hydride $\text{LiBH}_4\text{--LiI}$.¹⁴ Alternatively, treatment at elevated temperatures (150 °C) of LiBH_4 together with LiNH_2 leads to the formation of a new phase, $\text{Li}_2(\text{BH}_4)(\text{NH}_2)$. The formation of a new phase causes a conductivity enhancement and a relatively low phase transition temperature of approximately 50 °C.^{30,39} A main disadvantage of this method is, however, that the resulting compounds suffer from poor electrochemical and thermal cycling stability because of phase segregation.

The second approach, which has led to a large increase in the ionic conductivity in several classes of solid electrolytes, is interface engineering by forming nanocomposites with oxides such as SiO_2 and Al_2O_3 .^{40–43} This approach, especially when using carbon scaffolds, was originally proposed to enhance the hydrogen sorption properties of complex hydrides,^{44–48} but it was additionally shown to influence the ion mobility in the materials as well. The increase in ionic conductivity is currently believed to be caused by interactions of the hydride with the scaffold surface leading to either interfacial space charge zones⁴⁹ or to the formation of highly conducting compounds at this interface⁵⁰ due to changes in structure or defect density. The exact nature of the hydride/oxide interface is still a subject of intensive investigation. Alternatively, it has been shown that nanocrystalline LiBH_4 has an enhanced ionic conductivity compared to the microcrystalline form.⁵¹ Interface engineering of LiBH_4 is normally achieved by nanoconfinement, e.g., via melt infiltration⁵² of LiBH_4 in the nanopores of the oxides^{40,42} or by ball milling^{41–43} a mixture of LiBH_4 and the metal oxide. The two preparation methods have been reported to lead to comparable effects. Results from testing all-solid-state Li–S batteries using $\text{LiBH}_4/\text{SiO}_2$ nanocomposites as electrolytes showed that this approach enhances the ionic conductivity of LiBH_4 and leads to better electrochemical and cycling stability.^{53–55}

It has been shown that in these so-called dispersed ionic conductors, only the conductor or electrolyte (e.g., LiBH_4) near the interface with the oxide (within 1–2 nm) exhibits very high ion mobility at room temperature.^{48,55} Nevertheless, the volume fraction far from the interface is crucial to achieve interconnected LiBH_4 particles as the silica or alumina particles

do not contribute to the ionic conductivity. Only a percolating network of fast Li^+ diffusion pathways will guarantee facile Li ion transport over long distances. We hypothesize that the overall long-range ionic conductivity of the nanocomposite can be further improved if the conductive regions are interconnected via highly conductive Li^+ diffusion pathways rather than just bulk LiBH_4 .

For this purpose, we prepared nanoconfined anion substituted LiBH_4 . In these nanocomposites, the combined effects of partial anion substitution, either with I^- or NH_2^- , and nanoconfinement in metal oxides (SiO_2 and Al_2O_3) indeed leads to high room temperature Li-ion conductivities. In agreement with this observed enhancement, the activation energy for Li ion transport is lower than those probed for nanoconfined LiBH_4 and the unconfined anion-substituted ($\text{LiBH}_4\text{--LiI}$, $\text{LiBH}_4\text{--LiNH}_2$) systems. By using different preparation methods, we show that the enhancement seen for nanoconfined $\text{LiBH}_4\text{--LiI}$ and $\text{LiBH}_4\text{--LiNH}_2$ is indeed due to the combined effects of interfacial interactions with the metal oxide surface groups and the presence of highly conducting anion-substituted LiBH_4 located further away from the SiO_2 or Al_2O_3 surfaces. LiBH_4 was used as an excellent model system to demonstrate the effect of combining anion substitution and nanoconfinement, and we believe that this approach and outcome are applicable to a wide variety of solid-state electrolytes.

2. EXPERIMENTAL SECTION

Synthesis of Silica Supports. MCM-41 was synthesized using the procedure described by Cheng et al.⁵⁶ In brief, hexadecyltrimethylammonium bromide (Sigma-Aldrich, $\geq 96.0\%$) and tetramethylammonium hydroxide solution (Sigma-Aldrich, 25 wt % in H_2O) were mixed with deionized water. After the addition of the silica source (Aerosil 380), the white suspension was stirred for 2 h at 30 °C and kept at this temperature for another 24 h unstirred in a closed polypropylene bottle. The composition of the mixture was 1.00 SiO_2 : 0.19 (TMA)OH: 0.27 (CTA)Br: 40 H_2O . The jelly like product was heated to 140 °C in stainless steel autoclaves and kept there for 48 h. After being naturally cooled to room temperature, the mixture was thoroughly washed, filtered, and dried at 120 °C for approximately 12 h. The final calcination step (550 °C, 12 h) was carried out after heating the sample first to 100 °C for 1 h as an additional drying step.

SBA-15 was prepared according to Zhao et al.⁵⁷ Poly(ethylene glycol)-*block*-poly(propylene glycol)-*block*-poly(ethylene glycol) (Sigma-Aldrich, PEG–PPG–PEG, Pluronic, P-123), hydrochloric acid fuming 37% (Merck, for analysis), and deionized water were stirred at 35 °C. Tetraethyl orthosilicate (Sigma-Aldrich, $\geq 99.0\%$ GC, TEOS) was added dropwise to the solution, and the solution was then stirred for 24 h at 40 °C resulting in a composition of 0.015 P123:5.2 HCl: 129 H_2O : 1 TEOS. This mixture was kept at 100 °C in a closed polypropylene bottle for 48 h, followed by extensive washing and filtration. Subsequently, the product was predried (60 °C, 24 h, air), dried (120 °C, 8 h, air), and calcined (1.2 °C min^{-1} , 550 °C, 6 h, air).

Electrolyte Preparation. Alumina (Al_2O_3) was purchased from Sasol (product brand Puralox SCCa-5/200), while lithium amide (95% pure), lithium iodide (98% pure), and lithium borohydride (95% pure) were purchased from Sigma-Aldrich. The metal oxide supports (MCM-41, SBA-15 and Al_2O_3) were first dried under a vacuum at 220 °C overnight;

then we stored them in an Ar purified glovebox (MBraunLab-master, typically H_2O and $\text{O}_2 < 1$ ppm). All subsequent sample handling and transfer were carried out in the glovebox to avoid contamination with air or traces of moisture. The $\text{LiBH}_4\text{--LiI}$ /oxide nanocomposites were prepared using two different methods. In the first method, LiBH_4 and LiI were *physically mixed* in molar ratios of 10, 20, 30, and 40 mol % LiI with respect to LiBH_4 . Subsequently, the materials were mixed with the desired amount of the oxide and placed in a quartz reactor which was then inserted inside a stainless-steel high-pressure autoclave (Parr). The amounts were calculated in order to fill the oxide pores by 130%, meaning that all pores were filled and voids between particles and space between grains were filled additionally. Melt infiltration was carried out at 50 bar H_2 pressure and a temperature of 295 °C for 30 min; the heating rate was approximately 3 °C min^{-1} .⁴⁸ During this process, LiI--LiBH_4 forms a solid solution ($(1-x)\text{LiBH}_4\text{--}x\text{LiI}$ with $x = 0.1, 0.2, 0.3, 0.4$) which melts and infiltrates the pores of the oxide. Upon cooling, the molten solid solution solidifies in the pores of the support material, and the excess amount remains at the external surface of the support.

In the second approach, the samples were prepared by combining *solution impregnation* and melt infiltration. A solution of LiI and water or ethanol was prepared. The desired amount of the solution was added dropwise, using a syringe and a septum, to the metal oxide support contained in a round-bottom flask. This was done outside the glovebox but by using a Schlenk line to avoid contamination. The impregnated oxide was kept at room temperature for 3 h, after which the solvent was removed. Subsequently, the mixture was dried at 250 °C overnight under a dynamic vacuum. In order to reach the desired amount of LiI in the pores, the procedure was repeated twice. The LiI /metal oxide nanocomposite was mixed with LiBH_4 to reach a molar ratio LiI/LiBH_4 of 20:80 with the volume of $\text{LiBH}_4\text{--LiI}$ corresponding to 130% of the total pore volume of the silica (or alumina). The mixture was then inserted into a sample holder placed inside a stainless-steel high-pressure autoclave, pressurized to 50 bar H_2 and heated at 3 °C min^{-1} to 295 °C. The dwell time was 30 min. The molten LiBH_4 infiltrates the oxide pores and reacts with the nanoconfined LiI to form $\text{LiBH}_4\text{--LiI}$.

Reference samples of $\text{LiBH}_4\text{--LiI}$ solid solutions and nanoconfined LiBH_4 were prepared under the same autoclave conditions as outlined above. Solid solutions were synthesized by heating mixtures of LiBH_4 and LiI without adding the metal oxide support; nanoconfined LiBH_4 was obtained without adding LiI to the mixture. A third reference sample was bulk LiBH_4 , which was ground and melted under the same autoclave conditions and recrystallized.

$\text{LiBH}_4\text{--LiNH}_2$ /oxide nanocomposites were prepared using a two-step preparation method. First, LiBH_4 and LiNH_2 were physically mixed in a molar ratio of 50% LiNH_2 with respect to LiBH_4 . Afterward, the physical mixture was placed in a stainless-steel reactor which was then inserted into a stainless-steel high-pressure autoclave. The solid-state reaction was carried out at 50 bar H_2 pressure and at 150 °C (heating rate 2.5 °C min^{-1}) for 30 min to form a solid solution with the composition $0.5\text{LiBH}_4\text{--}0.5\text{LiNH}_2$. Subsequently, the solid solution was mixed with the desired amount of oxide in order to fill the pores by 130%. Melt infiltration was carried out at 50 bar H_2 pressure at 120 °C (2.5 °C min^{-1}) for 30 min. Upon cooling, the molten solid solution recrystallized in the

pores of the support material to form nanoconfined $\text{LiBH}_4\text{--LiNH}_2$.

Characterization of Pristine Materials and Composites. X-ray diffraction was performed with a Bruker-AXS D-8 Advance X-ray diffractometer with $\text{Co K}\alpha_{1,2}$ radiation ($\lambda = 1.79026$ Å). The samples were placed in an airtight sample holder, and diffractograms were recorded at room temperature covering a 2θ range of 10° to 100° for alumina-based samples and of 20 to 80° 2θ for the silica containing samples as well as the crystalline samples. The increment and scan duration per point was 0.12° 2θ and 4 s, respectively, for the alumina samples; 0.06° 2θ and 2 s, respectively, for the silica samples; and 0.03° 2θ and 1 s, respectively, for the crystalline samples. Rietveld refinement was carried out using the software X'PertHighScore Plus. A Le-Bail fit was applied to analyze the pattern; literature patterns of hexagonal LiBH_4 taken from the Inorganic Crystal Structure Database served as reference. To refine the patterns, we used the lattice parameters of hexagonal LiBH_4 as starting values ($a = 4.28$ Å, $b = 4.28$ Å, $c = 6.98$ Å).

Diffuse reflectance infrared Fourier transform spectra (DRIFTS) were obtained by a PerkinElmer 2000 spectrometer and a MCT detector. Sixteen scans were accumulated with a resolution of 4 cm^{-1} in the range of 500 to 4500 cm^{-1} . An airtight sample holder (KBr background) guaranteed no air contamination during the measurements. Data acquisition was realized by recording absorbance versus wavenumber. The absorbance is directly converted to K-M units, introduced by Kubelka and Munk, which includes a scattering component and is, therefore, typically used for the analysis of powder samples.

Conductivity Measurement. Alternating current (AC) impedance spectroscopy measurements were performed using a Princeton Applied Research Parstat 2273. Lithium foil (Sigma-Aldrich, 99.9%, 0.38 mm thick and 12 mm in diameter leading to a surface of 1.33 cm^2) was firmly placed on top of two 13 mm stainless steel dies. A 100–300 mg portion of the electrolyte was placed between the two lithium foils in a standard pellet die set. The sample was pressed using a pressure of 2 tons, resulting in a final electrolyte thickness of 1 to 2 mm, excluding the Li foil. With the weight of the samples, we calculated that the void fraction of the pellets is below 20%. The pressed sample pellet, which is tightly connected to the Li foils and stainless-steel dies, was placed in a custom-made impedance cell housed in a Büchi B-585 glass oven that was placed in an Ar-filled glovebox. The voltage amplitude of the AC signal was 1 V; we measured complex impedances over a frequency range from 1 MHz to 1 Hz. Generally, the pellets were heated from room temperature to 50 or 130 °C (depending on the sample), and then the samples were cooled down to room temperature. During this temperature cycle, impedance scans were acquired in steps of 5 or 10 °C. Before the acquisition of each scan, the measurement cell was allowed to equilibrate at the desired temperature for 45 min (while heating), 90 min (while cooling), and 150 min (for measurements at room temperature). The entire sequence was repeated for 2 to 3 cycles to investigate any hysteresis behavior and to detect any changes of the samples. Matlab and ZView software were used to fit the raw data by using Nyquist plots. A constant phase element (CPE) and a resistor connected in parallel were used as appropriate equivalent circuit to parametrize the data. Capacitances, C , were calculated according to $C = R^{(1-n)/n} \times Q^{1/n}$. R is the resistance

in Ω , i.e., it denotes the real part of the complex impedance; Q has the numerical value of the admittance at $\omega = 1 \text{ rad s}^{-1}$. n is a dimensionless variable characterizing the deviation of the CPE from the behavior of an ideal RC unit, which would yield $n = 1$.

NMR Line Shape Measurement. To underpin the findings by conductivity spectroscopy, we recorded ^7Li (spin-3/2) nuclear magnetic resonance (NMR) spectra at a magnetic field of 7 T, corresponding to a Larmor frequency of 116 MHz, by employing a Bruker Advance III solid-state spectrometer. We used a standard broadband probe to acquire variable-temperature NMR spectra with a one pulse sequence under static, i.e., nonrotating conditions. The $\pi/2$ pulse length slightly depended on temperature and ranged from 2.1 to 2.3 μs . Such short pulse lengths ensured nonselective excitation of the whole spectra. Up to 16 scans were accumulated to form an average free induction decay, which, after Fourier transformation, yield the ^7Li NMR spectra. The temperature in the sample chamber was monitored by a Eurotherm controller. Temperature adjustment was achieved, with an accuracy of $\pm 2\text{K}$, with a heater that was constantly flushed with a stream of dry nitrogen gas.

3. RESULTS AND DISCUSSION

Structure of $((1-x)\text{LiBH}_4\cdot x\text{LiI})$ and Its Nanoconfined Counterpart As Seen by XRD and DRIFTS. First, we discuss the structural properties of (i) the $\text{LiBH}_4\text{--LiI}$ solid solutions $((1-x)\text{LiBH}_4\cdot x\text{LiI})$ containing 10 to 40 mol % I ($x = 0.1, 0.2, 0.3$ and 0.4) and (ii) the nanocomposites with different oxides viz. $\gamma\text{-Al}_2\text{O}_3$, SBA-15, and MCM-41. The compositions of the samples in wt % are given in Table S1. Structural details of the hydrides, oxides, and nanocomposite materials are shown in Figure 1 as well as in Table S2 and Figures S1 to S6. Figure 1 shows the XRD powder pattern of a 20 mol % LiI--LiBH_4 solid solution and the patterns of the nanocomposites prepared using two different routes, i.e., comelt infiltration and impregnation with LiI followed by melt infiltration with LiBH_4 . For comparison, the XRD pattern of LiI and the patterns of orthorhombic and hexagonal LiBH_4 are also included. The influence of LiI on the on XRD patterns of the solid solutions and the composites is illustrated in Figures S7 and S8. The patterns shown here are normalized to the highest intensities; hkl values are added to distinct reflections of LiBH_4 ^{58,59} and LiI ,^{60–62} respectively. The XRD patterns of the $\text{LiBH}_4\text{--LiI}$ samples with 10 and 20 mol % LiI (Figure S7) clearly differ from those of orthorhombic LiBH_4 and LiI . Instead they resemble the pattern of hexagonal LiBH_4 being the stable phase at elevated temperatures. The reflections in the range from 27° to 32° 2θ are shifted toward lower 2θ values by approximately 1° 2θ . This shift reveals successful incorporation of LiI and is caused by lattice expansion because I^- is larger than BH_4^- .³⁵ A similar shift has been reported in literature.¹⁴ Rietveld refinement of the diffraction data for the $0.8\text{LiBH}_4\cdot 0.2\text{LiI}$ solid solution yielded an hcp unit cell with the following lattice parameters $a = 4.44 \text{ \AA}$, $b = 4.44 \text{ \AA}$, and $c = 7.19 \text{ \AA}$. Simultaneously with lattice expansion, the density increased from 0.67 g/cm^3 for bulk LiBH_4 to 1.20 g/cm^3 for $0.8\text{LiBH}_4\cdot 0.2\text{LiI}$. Samples with more than 20 mol % LiI revealed reflections of pure LiI indicating a solubility limit for the $\text{LiBH}_4\text{--LiI}$ system (Figure S7).

Confinement of the $\text{LiBH}_4\text{--LiI}$ solid solutions in the oxide nanopores led to both broadening and a decrease in intensity of the diffraction peaks (see Figures 1 and S8). Peak

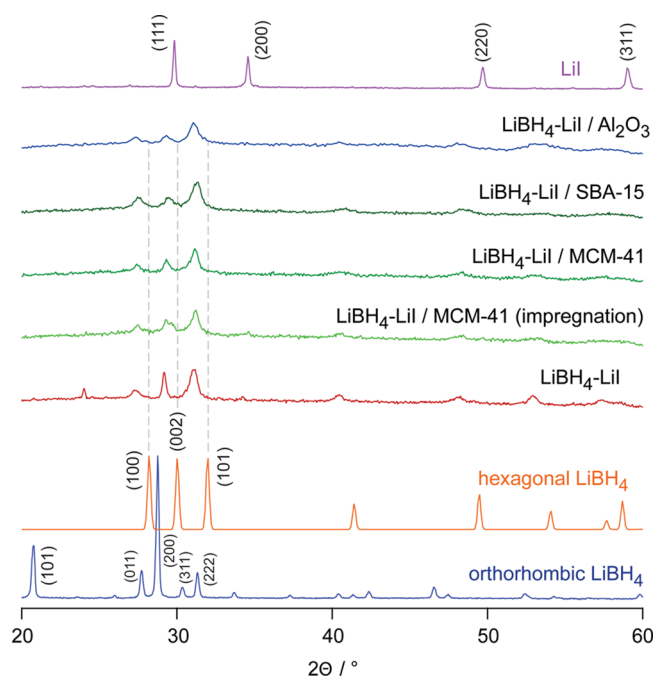


Figure 1. XRD powder patterns of the various $\text{LiBH}_4\text{--LiI}$ /oxide nanocomposites investigated. For comparison, the positions of the reflection of LiBH_4 in its hexagonal form are included as well. In addition, the pattern of $\text{LiBH}_4\text{--LiI}$ (20 mol % of LiI) and LiI are also shown. Values in brackets refer to hkl indices. The shift of the reflections toward lower diffraction angles indicates successful incorporation of LiI that stabilizes the hexagonal form of LiBH_4 .

broadening is expected because of size effects and lattice strain, whereas the decrease in intensity suggests a decrease in the long-range order. Note, however, that the composites shown here contain 30 vol % more $\text{LiBH}_4\text{--LiI}$ than is required to fill all the pores of the scaffold. This is essential for interconnectivity between the LiBH_4 particles. For the nanocomposites with $\text{LiBH}_4\text{--LiI} \leq 100\%$ of the total pore volume of the scaffold, no crystalline phase was observed. Thus, we conclude that nanoconfinement led to a significant decrease in crystallinity of the samples. The similarity in the diffraction patterns of the nanocomposites prepared using the different methods (Figure 1) suggests that both methods are useful for the preparation of $\text{LiBH}_4\text{--LiI}$ /metal oxide solutions. Moreover, the use of different oxide supports did not lead to major differences in the XRD patterns of the nanocomposites.

Further evidence for successful incorporation of the solid solutions into the oxide pores is provided by nitrogen physisorption measurements. The measurements showed that only a negligible amount of nitrogen was adsorbed by the nanocomposites. This finding proved that the pores were occupied by the electrolyte $\text{LiBH}_4\text{--LiI}$.

DRIFTS was used to investigate the nature of chemical bonding in the different samples prepared. In Figure 2 the spectrum of the $\text{LiBH}_4\text{--LiI}/\text{Al}_2\text{O}_3$ nanocomposite is compared to spectra of bulk LiBH_4 , $\text{LiBH}_4\text{--LiI}$, and pristine Al_2O_3 . The spectra are presented in arbitrary K-M units (for further explanation see the Experimental Section). Macrocrystalline, that is, bulk LiBH_4 , shows characteristic bands between 1000 and 1500 cm^{-1} which correspond to $[\text{BH}_4]^-$ bending vibrations; bands appearing in the range from 2000 to 2800 cm^{-1} can be associated with stretching vibrations in $[\text{BH}_4]^-$.^{63,64} The most preminent bands of LiBH_4 are marked

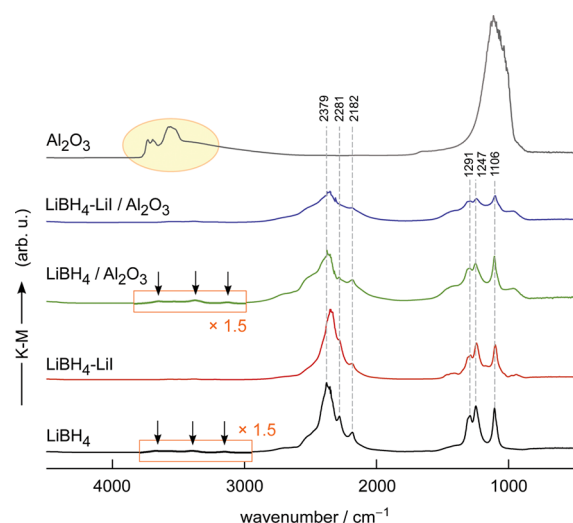


Figure 2. DRIFT spectra of Al_2O_3 , nanoconfined $\text{LiBH}_4\text{-LiI}/\text{Al}_2\text{O}_3$, nanoconfined $\text{LiBH}_4/\text{Al}_2\text{O}_3$, and $\text{LiBH}_4\text{-LiI}$ (20 mol % of LiI). For comparison, the spectrum of LiBH_4 is also shown. Main peaks are marked by vertically drawn dashed lines with the wavenumbers indicated. K-M intensities (see the ordinate axis) are in arbitrary units. See text for further explanation.

with dashed lines in gray color; the corresponding wavenumbers are indicated. The spectrum of the $\text{LiBH}_4\text{-LiI}$ solution resembles that of LiBH_4 , the band characterizing the stretching vibrations (2379 cm^{-1}) is, however, slightly shifted toward a lower wavenumber. Most likely, this shift is due to the effect of negative chemical pressure resulting from an increased unit cell by addition of I, as previously observed for halide-substituted BH_4 .⁶⁵ Also, a stronger electronic interaction between iodine and Li, because of the higher electronegativity of the halides compared to BH_4^- , can lead to such a change in vibration frequencies.⁶⁶ For $\text{LiBH}_4\text{-LiI}/\text{Al}_2\text{O}_3$, the bands are clearly broadened due to nanoconfinement. A similar broadening effect is also observed for $\text{LiBH}_4/\text{Al}_2\text{O}_3$. It suggests that the structure of the confined materials is different from the bulk compound. This observation is in line with previous studies on nanoconfined LiBH_4 .^{67–69}

Interestingly, the bands of Al_2O_3 in the region from 3400 to 3800 cm^{-1} , representing OH surface groups,⁷⁰ almost disappear after the pores are filled with electrolyte; see the vertical arrows in Figure 2. The same behavior is found for the characteristic vibrations of the surface OH-silanol groups of silica^{71,72} in the samples $\text{LiBH}_4/\text{SiO}_2$, LiI/SiO_2 , and $\text{LiBH}_4\text{-LiI}/\text{SiO}_2$ (see Figures S9 and S10). Interaction of LiBH_4 with the surface is the origin of the high ionic conductivity of $\text{LiBH}_4/\text{oxide}$ nanocomposites.

Ionic Conductivity of Nanoconfined $\text{LiBH}_4\text{-LiI}$. To evaluate the effects of different LiI concentrations on ionic conductivity, we recorded complex impedance data at different temperatures and analyzed the results in the Nyquist representation; see Figure 3. An overview of results from impedance spectroscopy of the $\text{LiBH}_4\text{-LiI}$ solid solutions and the nanocomposites is given in Table S3 and Figure S11. The overall ionic conductivity of the confined and pure solid solutions increased with increasing amounts of added LiI. At LiI contents higher than 20 mol %, the conductivity started to decrease (Figure S12). This is in line with results from XRD pointing to crystalline (unreacted) LiI above this composi-

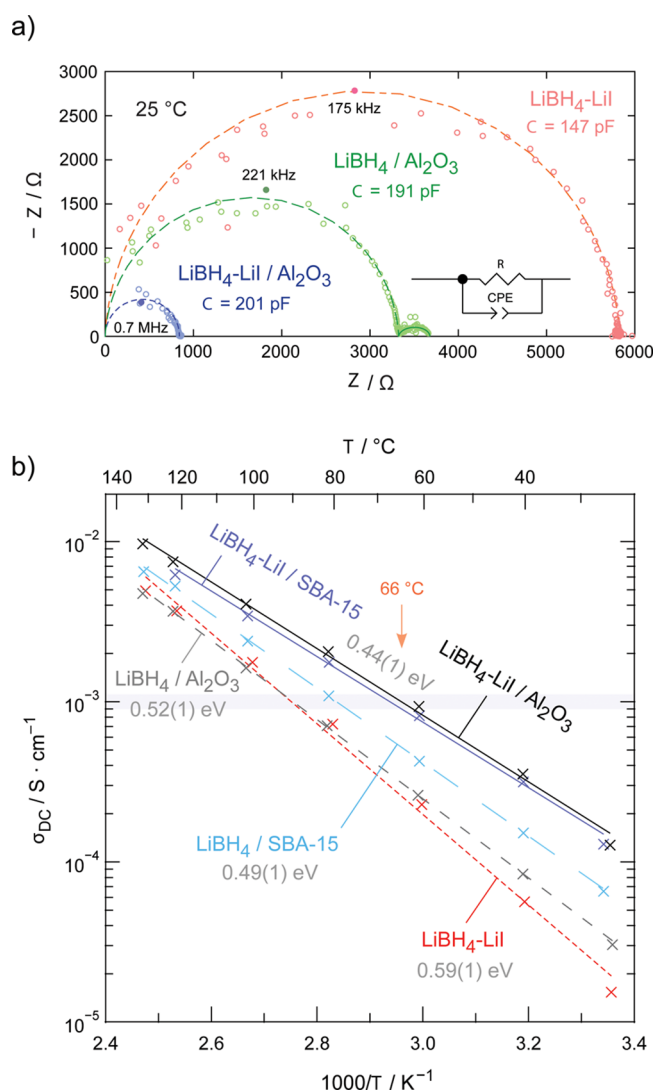


Figure 3. (a) Nyquist plots, that is, the imaginary part, $-Z''$, of the complex impedance plotted versus the real part Z' , of nanoconfined $\text{LiBH}_4\text{-LiI}/\text{Al}_2\text{O}_3$ and $\text{LiBH}_4/\text{Al}_2\text{O}_3$. The $\text{LiBH}_4\text{-LiI}$ sample (20 mol % LiI) is also shown. Values in pF show the capacitances obtained after parametrizing the main (nondepressed) semicircles with the equivalent circuit shown; see also Experimental section. The line approximating the second semicircle of the curve belonging to $\text{LiBH}_4/\text{Al}_2\text{O}_3$, which shows up at higher frequencies, is drawn to guide the eye. (b) Arrhenius plot (half-logarithmic plot of σ vs $1000/T$) to illustrate the change of conductivity with increasing temperature. Dashed and solid lines represent linear fits to determine activation energies E_A , which range from $0.44(1)\text{ eV}$ to $0.59(1)\text{ eV}$. Nanoconfined $\text{LiBH}_4\text{-LiI}/\text{Al}_2\text{O}_3$ shows the highest conductivities. At room temperature ($25\text{ }^\circ\text{C}$), its ion conductivity is slightly larger than 10^{-4} S cm^{-1} ; a conductivity of 10^{-3} S cm^{-1} , needed to realize Li-ion batteries, is reached at $66\text{ }^\circ\text{C}$.

tional limit. Hence, the sample LiI-LiBH_4 with 20 mol % LiI was chosen for a more detailed study.

Figure 3a shows the corresponding Nyquist plot recorded at $25\text{ }^\circ\text{C}$; in Figure 3b, the temperature dependence of the ionic conductivity is displayed using an Arrhenius plot. For comparison, the Nyquist plots and conductivity data referring to $\text{LiBH}_4\text{-LiI}$ and nanoconfined LiBH_4 are also shown. Capacitances C ranged from 147 to 210 pF; values larger than 100 pF typically indicate electrical relaxation processes influenced by interfacial regions.⁷³ For nanoconfined compo-

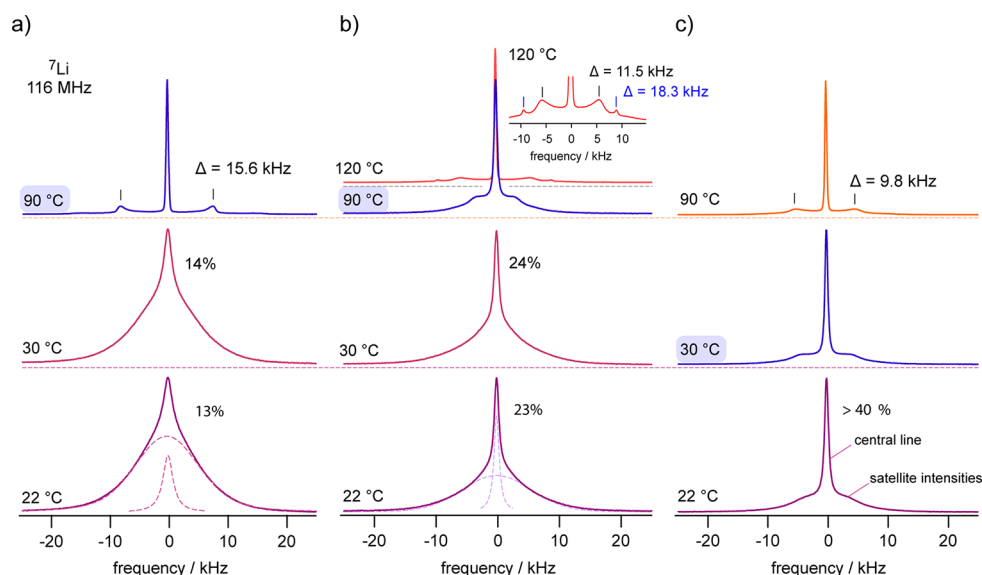


Figure 4. ^7Li NMR spectra of (a) $\text{LiBH}_4\text{-LiI}$, (b) nanoconfined $\text{LiBH}_4/\text{Al}_2\text{O}_3$ without LiI , and (c) nanoconfined $\text{LiBH}_4\text{-LiI}/\text{Al}_2\text{O}_3$. Spectra were recorded at a Larmor frequency of 116 MHz at the temperatures indicated. Dashed lines in parts a and b show the deconvolution of the entire line with appropriate Gaussian and Lorentzian functions to estimate the number fraction of mobile Li ions in these compounds. For $\text{LiBH}_4\text{-LiI}/\text{Al}_2\text{O}_3$, the spectrum has almost adopted its final form at temperatures as low as 30 °C. While the sharp line represents fast Li ions, the broader foot comprises both the central line of a fraction of slower Li ions and quadrupole intensities. The latter become visible as a sharp powder pattern at elevated temperature where dipole–dipole interactions are effectively averaged out due to rapid Li^+ exchange. See text for further information.

sites, it is widely believed that ion transport mainly occurs along the heterogeneous solid–solid interphase, that is, at the interface between the insulating oxide and the electrolyte.^{41–43}

The exponents n turned out to take values close to 1 meaning that the corresponding CPEs (constant phase elements) of all three samples behaved almost like an ideal RC unit. This observation is in line with the interpretation that the semicircle seen in the complex plane plot is governed by a response strongly influenced by grain boundary effects.

For $\text{LiBH}_4/\text{Al}_2\text{O}_3$, a second semicircle is seen at lower frequencies, which is either too small to be detected or is absent in $\text{LiBH}_4\text{-LiI}$ and $\text{LiBH}_4\text{-LiI}/\text{Al}_2\text{O}_3$. The presence of the second semicircle suggests two different conducting phases. We attribute the main semicircle with the higher electrical relaxation rate to LiBH_4 interacting with the oxide surface and the semicircle appearing at lower frequencies to LiBH_4 , which is farther away from the interface. This feature is also seen in ^7Li NMR spectroscopy; see Figure 4. We suppose that the addition of LiI led to both an increase of the high conducting regions and an enhancement of interfacial conductivity. Thus, for $\text{LiBH}_4\text{-LiI}/\text{Al}_2\text{O}_3$, the two contributions could not be resolved any longer when data recorded at 25 °C were analyzed.

The Arrhenius plot shown in Figure 3b shows that ion transport at temperatures lower than 100 °C is clearly faster in the nanocomposites $\text{LiBH}_4\text{-LiI}/\text{Al}_2\text{O}_3$ and $\text{LiBH}_4\text{-LiI}/\text{SiO}_2$ than in $\text{LiBH}_4\text{-LiI}$ and the nanoconfined samples $\text{LiBH}_4/\text{Al}_2\text{O}_3$ and $\text{LiBH}_4/\text{SiO}_2$. For instance, at room temperature (25 °C), the ionic conductivity of $\text{LiBH}_4\text{-LiI}/\text{Al}_2\text{O}_3$ (0.1 mS cm^{-1}) was four times higher than that of $\text{LiBH}_4/\text{Al}_2\text{O}_3$ and eight times higher than that of $\text{LiBH}_4\text{-LiI}$. In agreement with the trend for the increase in ionic conductivity, the activation energy for long-range ion transport decreased from 0.52(1) eV for $\text{LiBH}_4/\text{oxide}$ to 0.44(1) eV for $\text{LiBH}_4\text{-LiI}/\text{oxide}$. $\text{LiBH}_4\text{-LiI}$ showed a rather high activation energy of 0.59 eV. These

values are similar to those reported in literature for $\text{LiBH}_4/\text{Al}_2\text{O}_3$ and LiI-LiBH_4 systems.^{35,41}

^7Li NMR line shapes of these samples, which have been recorded at room temperature and above, clearly revealed that Li^+ acts as mobile charge carrier.⁷⁴ Selected lines are shown in Figure 4. For the $\text{LiBH}_4\text{-LiI}$ solid solution (see Figure 4a), the line at room temperature is composed of two contributions. The narrow line on top of the broader signal reflects the mobile Li spins whose jump rates exceed the line widths of this line in the rigid lattice, which turns out to be approximately 13 kHz. Narrow NMR lines are caused by sufficiently fast Li^+ exchange processes able to average local dipole–dipole interactions that lead to line broadening at low temperatures. In the case of $\text{LiBH}_4\text{-LiI}$, the line shape did not change much when going to 30 °C; however, a significant change was seen at 90 °C where a fully narrowed central line appeared, that is, on top of a quadrupole powder pattern. This distinct pattern, showing sharp 90° singularities separated by $\Delta = 15.6$ kHz, is characteristic for hexagonal $\text{LiBH}_4\text{-LiI}$. A similar situation is seen for nanoconfined $\text{LiBH}_4/\text{Al}_2\text{O}_3$ (see Figure 4b). However, the number fraction of rapid Li^+ ions was higher at 22 and 30 °C (24%) compared to that seen for nonconfined $\text{LiBH}_4\text{-LiI}$. This difference is in line with the slightly higher conductivity seen for $\text{LiBH}_4/\text{Al}_2\text{O}_3$. It is worth noting that the motionally narrowed spectra recorded at 90 °C and at 120 °C were governed by electric quadrupole intensities being different than those of bulk LiBH_4 and bulk $\text{LiBH}_4\text{-LiI}$. The spectra of nonconfined LiBH_4 and nonconfined $\text{LiBH}_4\text{-LiI}$ reveal patterns produced by a symmetric electric field gradient (EFG) the ions were subjected to. They agree with those of similar systems studied earlier.⁴⁰

In contrast to the nonconfined samples, the NMR line of nanoconfined $\text{LiBH}_4/\text{Al}_2\text{O}_3$ recorded at 90 °C shows a nonsymmetric EFG. Its shape points to structural disorder and strain which the Li spins sense. Δ reduces from 15.6 to 11.5 kHz. Careful inspection of the powder pattern shows that

another set of singularities is present (see inset of Figure 4b), which is characterized by $\Delta = 18.3$ kHz. Assuming axial symmetry for this pattern, we obtained a quadrupole coupling constant δ_q of ca. 36.6 kHz which was identical to that of bulk LiBH_4 ($\delta_q = 37$ kHz).⁷⁵ The two quadrupole patterns represent the Li ions near the insulator surface ($\Delta = 11.5$ kHz) and the ions farther away, that is, located in the bulk regions ($\Delta = 18.3$ kHz). NMR revealed that these two species are exposed to different electric interactions. Two sources of electrical relaxation have also been seen in the corresponding Nyquist plot, vide supra.

For nanoconfined $\text{LiBH}_4\text{--LiI}/\text{Al}_2\text{O}_3$ (Figure 4c), we also observed a quadrupole powder pattern that is characterized by a lower Δ ($= 9.5$ kHz) than that expected for bulk $\text{LiBH}_4\text{--LiI}$. However, a pronounced pattern attributable to Li ions in bulk $\text{LiBH}_4\text{--LiI}$, as seen for $\text{LiBH}_4/\text{Al}_2\text{O}_3$, was missing. Instead, already at temperatures as low as 30 °C, an almost fully narrowed ^7Li NMR line was observed which clearly points to very fast ion dynamics in this nanocomposite.⁷⁴ We conclude that the majority of ions in this nanocomposite take part in rapid Li^+ exchange, which perfectly agrees with the conductivity trend seen in Figure 3b. From a structural point of view, the single EFG pattern observed points to a homogeneous sample as compared to nanoconfined $\text{LiBH}_4/\text{Al}_2\text{O}_3$. Presumably, if the ions reside in areas farther away from the surface of the oxide, they are subjected to a structurally stressed $\text{LiBH}_4\text{--LiI}$ phase with high ionic conductivity. This modified region, e.g., influenced by space charge zones, regions with higher defect density or increased structural disorder, may extend over almost the whole $\text{LiBH}_4\text{--LiI}$ phase leading to the enhancement in conductivity observed.

Note that all our samples were prepared under the same conditions and, therefore, the remarkable increase in ionic conduction for $\text{LiBH}_4\text{--LiI}/\text{Al}_2\text{O}_3$ seen by impedance spectroscopy and ^7Li NMR is mainly attributed to the combined effects of anion substitution and interface engineering by nanoconfinement. Table 1 compares conductivities, activation

energies, and Arrhenius prefactors of the samples investigated. The slight differences in ionic conductivity of the nano-composites prepared with different oxides (SBA-15, MCM-41, or Al_2O_3) are most likely due to differences in properties of these materials (see Figures S1 to S6 and Table S2). For example, the oxides differ in morphology, pore size, and pore size distribution, surface area, surface/interface energy, density of the surface groups, and the nature of the pores (e.g., pore corrugations). Detailed elucidation of the exact influence of these properties on ionic conductivity is, however, beyond the scope of the present work.

Importance of $\text{LiBH}_4\text{--LiI}$ /Oxide Interface. To further demonstrate that both the interaction of LiBH_4 with the oxide interface and partial anion substitution are important for the enhancement in ionic conductivity, we employed a preparation technique that is supposed to hinder the interaction of LiBH_4 with the oxide interface but still form $\text{LiBH}_4\text{--LiI}$ in the pores. This comparison showed that the nanocomposites prepared by coinfiltration of a physical mixture of LiBH_4 and LiI exhibited much higher conductivities than those which were prepared via solution impregnation (Table 1). If we first add LiI to fill the pores via impregnation with $\text{LiI}/\text{H}_2\text{O}$ or $\text{LiI}/\text{C}_2\text{H}_5\text{OH}$ solution and then add LiBH_4 by melt infiltration as a second step, we see that the resulting ionic conductivity is significantly lower. At first glance, this difference is surprising as results from XRD and IR (DRIFTS) suggest that both samples have similar structures (cf. Figure 1 and Figure S9). We attribute the marked change seen in conductivity to the fact that if LiI is added first, we do not have the original SiOH groups present at the interface anymore (see Figure S9 for the loss of silanol groups in LiI/SiO_2). This changed the properties of the interface with the LiBH_4 , and as a result, the conductivity is not as high as that with the other preparation technique.

$\text{LiBH}_4\text{--LiNH}_2$ System. To demonstrate the general applicability of the strategy outlined above, we measured also the conductivity of another nanoconfined electrolyte containing two complex anions, i.e., nanoconfined $\text{LiBH}_4\text{--LiNH}_2$. XRD revealed the formation of two new phases, namely, $\text{Li}_2(\text{BH}_4)(\text{NH}_2)$ and $\text{Li}_4(\text{BH}_4)(\text{NH}_2)_3$ (see Figure 5a). This is unlike the $\text{LiBH}_4\text{--LiX}$ systems where the high temperature phase of LiBH_4 was stabilized through the replacement of BH_4^- by halides causing lattice strain but no change in crystal structure. For nanoconfined $\text{LiBH}_4\text{--LiNH}_2/\text{MCM-41}$, XRD points to a loss of crystallinity, that is, long-range order. As mentioned above, the same feature was observed for the $\text{LiBH}_4\text{--LiI}$ solid solutions. In addition, results from DRIFTS measurements (see Figure 5b) revealed that the characteristic vibrations related to $\text{LiBH}_4\text{--LiNH}_2$, (1000 to 1500 cm^{-1} and 2000 to 2800 cm^{-1} (BH_4^-), 1500 to 1600 cm^{-1} and 3200 to 3300 cm^{-1} (NH_2^-), shifted toward lower wavenumbers and became significantly broader upon nanoconfinement. The bands related to the surface silanol groups (3700 cm^{-1}) were absent, as seen for nanoconfined $\text{LiBH}_4\text{--LiI}$. Hence, we conclude that the $\text{LiBH}_4\text{--LiNH}_2$ composite was successfully infiltrated into the nanopores of MCM-41 leading to profound changes of its structure.⁶⁶

In Figure 6, the ionic conductivities of selected $\text{LiBH}_4\text{--LiNH}_2$ samples are shown. First, when compared to LiBH_4 , it is clear that the addition of LiNH_2 to LiBH_4 increases the room temperature ionic conductivity by approximately 2 orders of magnitude. This increase is ascribed to the formation of $\text{Li}_2(\text{BH}_4)(\text{NH}_2)$.³⁹ The sudden increase in conductivity of $\text{Li}_2(\text{BH}_4)(\text{NH}_2)$ at approximately 35 °C originates from a

Table 1. Room Temperature Conductivities (σ) of the Samples Studied by Impedance Spectroscopy^d

sample	σ (25 °C) (S cm^{-1})	E_A (eV)	$\log_{10}(A)$ (S cm^{-1}K)
$\text{LiBH}_4/\text{MCM-41}$	2.29×10^{-5}	0.49(2)	6.0(3)
$\text{LiBH}_4\text{--LiI}/\text{MCM-41}$ comelt infiltration	3.86×10^{-5}	0.43(1)	5.3(1)
$\text{LiBH}_4\text{--LiI}/\text{MCM-41}$ impregnation (H_2O)	1.63×10^{-5}	0.52(2)	6.5(3)
$\text{LiBH}_4\text{--LiI}/\text{MCM-41}$ impregnation (EtOH)	4.57×10^{-6}	0.47(0)	5.2(1)
$\text{LiBH}_4\text{--LiI}/\text{SBA-15}$ comelt infiltration	1.29×10^{-4}	0.44(1)	6.0(2)
$\text{LiBH}_4\text{--LiI}/\text{Al}_2\text{O}_3$ comelt infiltration	1.27×10^{-4}	0.44(1)	6.1(1)
$\text{LiBH}_4\text{--LiI}$	1.54×10^{-5}	0.59(2)	7.8(3)
$\text{LiBH}_4\text{--LiNH}_2$	2.92×10^{-6}	1.03(1) ^a 0.19(1) ^b	1.8(1) ^a 13(1) ^b
$\text{LiBH}_4\text{--LiNH}_2/\text{MCM-41}$	1.16×10^{-4}	0.43(1) ^c	5.5(2)

^a E_A determined in the temperature range from 30 to 50 °C. ^b E_A determined in the temperature range from 60 to 85 °C. ^c E_A determined in the temperature range from 30 to 85 °C. ^dThe table also includes activation energies (E_A) and pre-factors ($\log_{10}(A)$) of the Arrhenius laws used to approximate the temperature dependence of the ionic conductivity. If not stated otherwise, E_A has been determined in the temperature range from 25 to 130 °C.

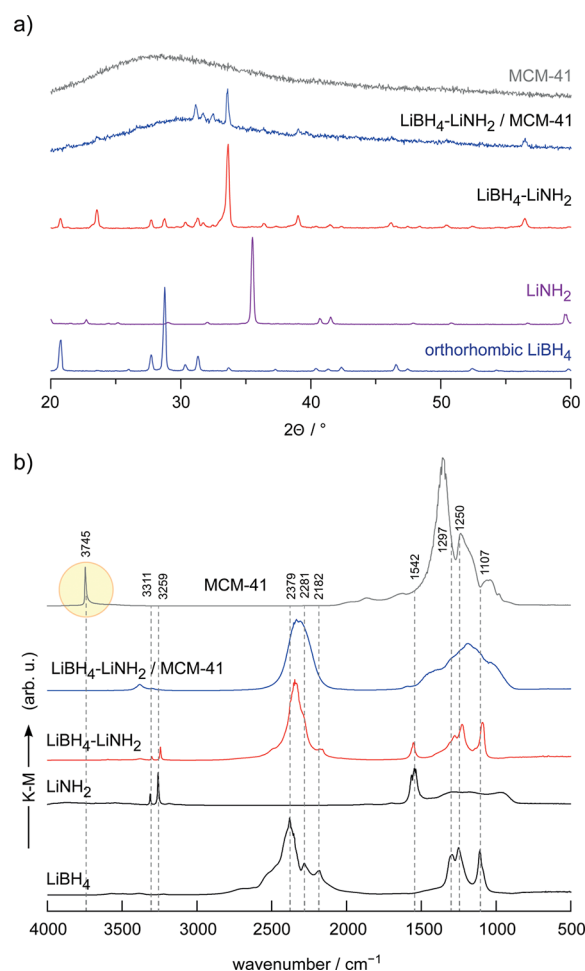


Figure 5. (a) X-ray powder diffraction patterns of nanoconfined and nonconfined $\text{LiBH}_4\text{-LiNH}_2$. For comparison, the expected patterns of orthorhombic LiBH_4 and LiNH_2 are also shown. The pattern at the top represents that of the oxide substrate, SiO_2 . (b) DRIFT spectra of the samples shown in part a; the spectra reveal broadening of the signals, which shift toward lower wavenumbers upon nanoconfinement. Those bands which result from silanol OH groups are absent for $\text{LiBH}_4\text{-LiNH}_2/\text{SiO}_2$ indicating surface reactions between the electrolyte and the surface of the oxide. See text for further explanation.

structural phase change leading to a highly conducting phase at temperature higher than 40 °C. Nanoconfined $\text{LiBH}_4\text{-LiNH}_2/\text{MCM-41}$ showed an even better ionic conductivity at this temperature; remarkably, this high ionic conductivity was also preserved at lower temperatures. When compared to LiBH_4 and $\text{LiBH}_4\text{-LiNH}_2$, the room temperature ionic conductivity of nanoconfined $\text{LiBH}_4\text{-LiNH}_2/\text{MCM-41}$ was higher by 4 and 2 orders of magnitude, respectively. It also exceeded that of nanoconfined $\text{LiBH}_4/\text{MCM-41}$ by a factor of 2 if conductivities at $T = 30$ °C were considered (cf. Figure 6). At approximately 50 °C, $\text{LiBH}_4\text{-LiNH}_2/\text{MCM-41}$ reached a conductivity of 1 mS cm^{-1} . Below 45 °C, the overall activation energy governing ion transport in $\text{LiBH}_4\text{-LiNH}_2/\text{MCM-41}$ (0.43 eV) is comparable to that of bulk LiBH_4 and significantly lower than that of $\text{LiBH}_4\text{-LiNH}_2$ at room temperature. For $\text{LiBH}_4/\text{MCM-41}$ and $\text{LiBH}_4\text{-LiNH}_2$ at higher temperatures, we see that E_A is somewhat lower, 0.26 and 0.19 eV, respectively; see Figure 6 and Table 1. On the basis of the results from the DRIFTS measurements, the remarkable

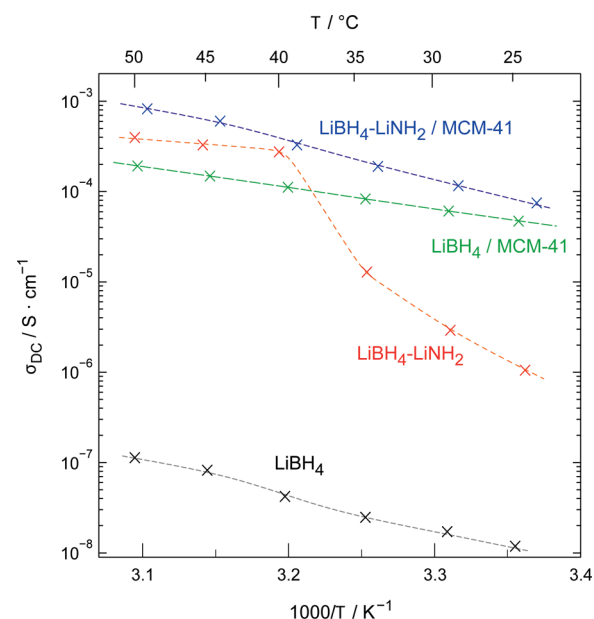


Figure 6. Ionic conductivity of nanoconfined $\text{LiBH}_4\text{-LiNH}_2/\text{SiO}_2$ as a function of the inverse temperature. For comparison, data on $\text{LiBH}_4/\text{SiO}_2$, nonconfined $\text{LiBH}_4\text{-LiNH}_2$ and bulk LiBH_4 are also included. The lines are to guide the eye.

increase in ionic conductivity is again attributed to the combined effect of anion substitution and interface effects, as observed for nanoconfined $\text{LiBH}_4\text{-LiI}$. These results illustrate that the synergistic effects of nanoconfinement, that is, interface engineering, and partial ion substitution is applicable to different Li-based electrolytes in various nonconducting nanoporous scaffolds.

4. CONCLUSION

We have shown how two routes, namely, ion substitution and interface engineering, can be effectively combined to enhance the ionic conductivity of solid-state electrolytes. Using complex hydrides as model systems, we developed an approach where anion substituted LiBH_4 ($\text{Li}_2(\text{BH}_4)_x\text{I}_{1-x}$ and $\text{Li}_2(\text{BH}_4)_x(\text{NH}_2)_{1-x}$) are confined in nanoporous SiO_2 or Al_2O_3 in order to exploit both the effect of ion substitution and nanoconfinement or interface engineering to boost the Li-ion conductivities of LiBH_4 at ambient conditions. Indeed, the ionic conductivity of the nanocomposites of $\text{LiBH}_4\text{-LiI}/\text{Al}_2\text{O}_3$ reached 0.1 mS cm^{-1} at room temperature. The room temperature conductivities of nonsubstituted $\text{LiBH}_4/\text{Al}_2\text{O}_3$ and $\text{LiBH}_4\text{-LiI}$ without nanoconfinement were 1 order of magnitude lower. Activation energies are in line with this trend, with 0.44, 0.52, and 0.59 eV for the $\text{LiBH}_4\text{-LiI}/\text{Al}_2\text{O}_3$, $\text{LiBH}_4/\text{Al}_2\text{O}_3$, and $\text{LiBH}_4\text{-LiI}$, respectively. Detailed structural investigations and ^7Li NMR line shape measurements show that the combined effects of interaction with the interface of the oxides and phase stabilization due to partial anion substitution (by the iodide anion) produces faster Li^+ diffusion pathways in $\text{LiBH}_4\text{-LiI}/\text{oxide}$ than those in the case of $\text{LiBH}_4/\text{oxide}$ and $\text{LiBH}_4\text{-LiI}$. Results on $\text{LiBH}_4\text{-LiNH}_2$ confined in mesoporous silica (MCM-41) show that this concept is also applicable to other Li-bearing hydrides. The enhancement effect depends also on the type and property of the scaffold. Our study clearly shows that combining partial anion substitution and nanoconfinement is a very promising

approach to achieve high room temperature ionic conductivities in solid-state ion conductors.

■ ASSOCIATED CONTENT

Supporting Information

The Supporting Information is available free of charge at <https://pubs.acs.org/doi/10.1021/acs.jpcc.9b10607>.

Calculation of the amount of material needed for melt infiltration to reach the desired pore filling; physisorption data; high-resolution scanning electron microscopy images; additional XRD patterns and DRIFTS data; further conductivity Arrhenius plot comparing different supports; comparison of room temperature conductivity values of samples with varying LiI content (0 to 40 mol %) (PDF)

■ AUTHOR INFORMATION

Corresponding Authors

Petra E. de Jongh – *Inorganic Chemistry and Catalysis, Debye Institute for Nanomaterials Science, Utrecht University, 3584 CG Utrecht, Netherlands*; orcid.org/0000-0002-2216-2620; Email: P.E.deJongh@uu.nl

Peter Ngene – *Inorganic Chemistry and Catalysis, Debye Institute for Nanomaterials Science, Utrecht University, 3584 CG Utrecht, Netherlands*; orcid.org/0000-0003-3691-0623; Email: P.ngene@uu.nl

Authors

Roman Zettl – *Institute for Chemistry and Technology of Materials, and Christian Doppler Laboratory for Lithium Batteries, Graz University of Technology (NAWI Graz), 8010 Graz, Austria; Inorganic Chemistry and Catalysis, Debye Institute for Nanomaterials Science, Utrecht University, 3584 CG Utrecht, Netherlands*

Laura de Kort – *Inorganic Chemistry and Catalysis, Debye Institute for Nanomaterials Science, Utrecht University, 3584 CG Utrecht, Netherlands*

Maria Gombotz – *Institute for Chemistry and Technology of Materials, and Christian Doppler Laboratory for Lithium Batteries, Graz University of Technology (NAWI Graz), 8010 Graz, Austria*

H. Martin R. Wilkening – *Institute for Chemistry and Technology of Materials, and Christian Doppler Laboratory for Lithium Batteries, Graz University of Technology (NAWI Graz), 8010 Graz, Austria*; orcid.org/0000-0001-9706-4892

Complete contact information is available at:

<https://pubs.acs.org/doi/10.1021/acs.jpcc.9b10607>

Author Contributions

R.Z. and L.d.K. contributed equally to this work.

Notes

The authors declare no competing financial interest.

■ ACKNOWLEDGMENTS

We greatly appreciate funding from the NWO materials for sustainability (Mat4Sus-739.017.009) and NWO-ECHO (712.015.005) grants. P.N. received funding from the European Research Council (ERC) under the European Union's Horizon 2020 research and innovation programme (ERC-2014-CoG No 648991). R.Z. and H.M.R.W. thank the Austrian Federal Ministry for Science, Research and Economy

as well as the Christian-Doppler Forschungsgesellschaft for financial support; further support by the FFG (The Austrian Research Promotion Agency) in the frame of the project Safe Battery is also acknowledged. R.Z. thanks the project SOLABAT (project no. 853627) funded by the Klima- und Energiefonds of FFG for additional support. Furthermore, we thank Sander Lambregts and Hans Meeldijk for physisorption and SEM measurements as well as Oscar Brandt Corstius for the synthesis of MCM-41.

■ REFERENCES

- (1) Manthiram, A.; Yu, X. W.; Wang, S. F. Lithium battery chemistries enabled by solid-state electrolytes. *Nat. Rev. Mater.* **2017**, *2* (4), 16103.
- (2) Janek, J.; Zeier, W. G. A solid future for battery development. *Nat. Energy* **2016**, *1*, 16141.
- (3) Mikhaylik, Y. V.; Akridge, J. R. Polysulfide shuttle study in the Li/S battery system. *J. Electrochem. Soc.* **2004**, *151* (11), A1969–A1976.
- (4) Kim, J. G.; Son, B.; Mukherjee, S.; Schuppert, N.; Bates, A.; Kwon, O.; Choi, M. J.; Chung, H. Y.; Park, S. A review of lithium and non-lithium based solid state batteries. *J. Power Sources* **2015**, *282*, 299–322.
- (5) Sun, C. W.; Liu, J.; Gong, Y. D.; Wilkinson, D. P.; Zhang, J. J. Recent advances in all-solid-state rechargeable lithium batteries. *Nano Energy* **2017**, *33*, 363–386.
- (6) Knauth, P. Inorganic solid Li ion conductors: An overview. *Solid State Ionics* **2009**, *180* (14–16), 911–916.
- (7) Takada, K. Progress and prospective of solid-state lithium batteries. *Acta Mater.* **2013**, *61* (3), 759–770.
- (8) Li, J. C.; Ma, C.; Chi, M. F.; Liang, C. D.; Dudney, N. J. Solid electrolyte: the key for high-voltage lithium batteries. *Adv. Energy Mater.* **2015**, *5* (4), 1401408.
- (9) Thangadurai, V.; Narayanan, S.; Pinzaru, D. Garnet-type solid-state fast Li ion conductors for Li batteries: Critical review. *Chem. Soc. Rev.* **2014**, *43* (13), 4714–4727.
- (10) Bohnke, O.; Bohnke, C.; Fourquet, J. L. Mechanism of ionic conduction and electrochemical intercalation of lithium into the perovskite lanthanum lithium titanate. *Solid State Ionics* **1996**, *91*, 21–31.
- (11) Li, J.; Lin, Y.; Yao, H. H.; Yuan, C. F.; Liu, J. Tuning thin-film electrolyte for lithium battery by grafting cyclic carbonate and combed poly(ethylene oxide) on polysiloxane. *ChemSusChem* **2014**, *7* (7), 1901–1908.
- (12) Hayashi, A.; Sakuda, A.; Tatsumisago, M. Development of sulfide solid electrolytes and interface formation processes for bulk-type all-solid-state Li and Na batteries. *Front. Energy Res.* **2016**, *4*, 25.
- (13) de Jongh, P. E.; Blanchard, D.; Matsuo, M.; Udovic, T. J.; Orimo, S. Complex hydrides as room-temperature solid electrolytes for rechargeable batteries. *Appl. Phys. A: Mater. Sci. Process.* **2016**, *122*, 251.
- (14) Matsuo, M.; Orimo, S. Lithium fast-ionic conduction in complex hydrides: review and prospects. *Adv. Energy Mater.* **2011**, *1* (2), 161–172.
- (15) Lu, Z. H.; Ciucci, F. Metal borohydrides as electrolytes for solid-state Li, Na, Mg, and Ca batteries: A first-principles study. *Chem. Mater.* **2017**, *29* (21), 9308–9319.
- (16) Möller, K.; Sheppard, D.; Ravnsbæk, D.; Buckley, C.; Akiba, E.; Li, H.-W.; Jensen, T. Complex metal hydrides for hydrogen, thermal and electrochemical energy storage. *Energies* **2017**, *10* (10), 1645.
- (17) Yoshida, K.; Sato, T.; Unemoto, A.; Matsuo, M.; Ikeshoji, T.; Udovic, T. J.; Orimo, S. Fast sodium ionic conduction in Na₂B₁₀H₁₀-Na₂B₁₂H₁₂ pseudo-binary complex hydride and application to a bulk-type all-solid-state battery. *Appl. Phys. Lett.* **2017**, *110* (10), 103901.
- (18) Sakintuna, B.; Lamari-Darkrim, F.; Hirscher, M. Metal hydride materials for solid hydrogen storage: A review. *Int. J. Hydrogen Energy* **2007**, *32* (9), 1121–1140.

- (19) Zuttel, A.; Wenger, P.; Rentsch, S.; Sudan, P.; Mauron, P.; Emmenegger, C. LiBH_4 a new hydrogen storage material. *J. Power Sources* **2003**, *118* (1–2), 1–7.
- (20) Umegaki, T.; Yan, J. M.; Zhang, X. B.; Shioyama, H.; Kuriyama, N.; Xu, Q. Boron- and nitrogen-based chemical hydrogen storage materials. *Int. J. Hydrogen Energy* **2009**, *34* (5), 2303–2311.
- (21) Schuth, F.; Bogdanovic, B.; Felderhoff, M. Light metal hydrides and complex hydrides for hydrogen storage. *Chem. Commun.* **2004**, *20*, 2249–2258.
- (22) Duchene, L.; Kuhnle, R. S.; Stilp, E.; Cuervo Reyes, E.; Remhof, A.; Hagemann, H.; Battaglia, C. A stable 3 V all-solid-state sodium-ion battery based on a closo-borate electrolyte. *Energy Environ. Sci.* **2017**, *10* (12), 2609–2615.
- (23) Asakura, R.; Duchene, L.; Kuhnle, R. S.; Remhof, A.; Hagemann, H.; Battaglia, C. Electrochemical oxidative stability of hydroborate-based solid state electrolytes. *ACS Appl. Energy Mater.* **2019**, *2* (9), 6924–6930.
- (24) Kim, S.; Oguchi, H.; Toyama, N.; Sato, T.; Takagi, S.; Otomo, T.; Arunkumar, D.; Kuwata, N.; Kawamura, J.; Orimo, S. A complex hydride lithium superionic conductor for high-energy-density all-solid-state lithium metal batteries. *Nat. Commun.* **2019**, *10*, 1081.
- (25) Matsuo, M.; Nakamori, Y.; Orimo, S.; Maekawa, H.; Takamura, H. Lithium superionic conduction in lithium borohydride accompanied by structural transition. *Appl. Phys. Lett.* **2007**, *91* (22), 224103.
- (26) Soulié, J. P.; Renaudin, G.; Černý, R.; Yvon, K. Lithium borohydride LiBH_4 : I. Crystal structure. *J. Alloys Compd.* **2002**, *346* (1), 200–205.
- (27) Aeberhard, P. C.; Refson, K.; David, W. I. F. Molecular dynamics investigation of the disordered crystal structure of hexagonal LiBH_4 . *Phys. Chem. Chem. Phys.* **2013**, *15* (21), 8081–8087.
- (28) Matsuo, M.; Takamura, H.; Maekawa, H.; Li, H. W.; Orimo, S. Stabilization of lithium superionic conduction phase and enhancement of conductivity of LiBH_4 by LiCl addition. *Appl. Phys. Lett.* **2009**, *94* (8), 084103.
- (29) Oguchi, H.; Matsuo, M.; Hummelshøj, J. S.; Vegge, T.; Nørskov, J. K.; Sato, T.; Miura, Y.; Takamura, H.; Maekawa, H.; Orimo, S. Experimental and computational studies on structural transitions in the LiBH_4 -LiI pseudobinary system. *Appl. Phys. Lett.* **2009**, *94* (14), 141912.
- (30) Matsuo, M.; Remhof, A.; Martelli, P.; Caputo, R.; Ernst, M.; Miura, Y.; Sato, T.; Oguchi, H.; Maekawa, H.; Takamura, H.; et al. Complex hydrides with $(\text{BH}_4)^-$ and $(\text{NH}_2)^-$ anions as new lithium fast-ion conductors. *J. Am. Chem. Soc.* **2009**, *131* (45), 16389.
- (31) Yao, Z. P.; Kim, S.; Michel, K.; Zhang, Y. S.; Aykol, M.; Wolverton, C. Stability and conductivity of cation- and anion-substituted LiBH_4 -based solid-state electrolytes. *Phys. Rev. Mater.* **2018**, *2* (6), 065402.
- (32) Mezaki, T.; Kuronuma, Y.; Oikawa, I.; Kamegawa, A.; Takamura, H. Li-ion conductivity and phase stability of Ca-doped LiBH_4 under high pressure. *Inorg. Chem.* **2016**, *55* (20), 10484–10489.
- (33) Ley, M. B.; Jorgensen, M.; Cerny, R.; Filinchuk, Y.; Jensen, T. R. From $\text{M}(\text{BH}_4)_3$ ($\text{M} = \text{La}, \text{Ce}$) Borohydride frameworks to controllable synthesis of porous hydrides and ion conductors. *Inorg. Chem.* **2016**, *55* (19), 9748–9756.
- (34) Rude, L. H.; Groppo, E.; Arnbjerg, L. M.; Ravnsbaek, D. B.; Malmkjær, R. A.; Filinchuk, Y.; Baricco, M.; Besenbacher, F.; Jensen, T. R. Iodide substitution in lithium borohydride, LiBH_4 -LiI. *J. Alloys Compd.* **2011**, *509* (33), 8299–8305.
- (35) Miyazaki, R.; Karahashi, T.; Kumatani, N.; Noda, Y.; Ando, M.; Takamura, H.; Matsuo, M.; Orimo, S.; Maekawa, H. Room temperature lithium fast-ion conduction and phase relationship of LiI stabilized LiBH_4 . *Solid State Ionics* **2011**, *192* (1), 143–147.
- (36) Sveinbjörnsson, D.; Myrdal, J. S. G.; Blanchard, D.; Bentzen, J. J.; Hirata, T.; Mogensen, M. B.; Norby, P.; Orimo, S. I.; Vegge, T. Effect of heat treatment on the lithium ion conduction of the LiBH_4 -LiI solid solution. *J. Phys. Chem. C* **2013**, *117* (7), 3249–3257.
- (37) Maekawa, H.; Matsuo, M.; Takamura, H.; Ando, M.; Noda, Y.; Karahashi, T.; Orimo, S. I. Halide-stabilized LiBH_4 , a room-temperature lithium fast-ion conductor. *J. Am. Chem. Soc.* **2009**, *131* (3), 894.
- (38) Stephenson, C. C.; Rice, D. W.; Stockmayer, W. H. Order-disorder transitions in the alkali borohydrides. *J. Chem. Phys.* **1955**, *23* (10), 1960–1960.
- (39) Yan, Y. G.; Kuhnle, R. S.; Remhof, A.; Duchene, L.; Reyes, E. C.; Rentsch, D.; Lodziana, Z.; Battaglia, C. A lithium amide-borohydride solid-state electrolyte with lithium-ion conductivities comparable to liquid electrolytes. *Adv. Energy Mater.* **2017**, *7* (19), 1700294.
- (40) Blanchard, D.; Nale, A.; Sveinbjörnsson, D.; Eggenhuisen, T. M.; Verkuijlen, M. H. W.; Suwarno; Vegge, T.; Kentgens, A. P. M.; de Jongh, P. E. Nanoconfined LiBH_4 as a fast lithium ion conductor. *Adv. Funct. Mater.* **2015**, *25* (2), 184–192.
- (41) Epp, V.; Wilkening, M. Motion of Li^+ in nanoengineered LiBH_4 and $\text{LiBH}_4\text{:Al}_2\text{O}_3$ comparison with the microcrystalline form. *ChemPhysChem* **2013**, *14* (16), 3706–3713.
- (42) Choi, Y. S.; Lee, Y. S.; Oh, K. H.; Cho, Y. W. Interface-enhanced Li ion conduction in a LiBH_4 - SiO_2 solid electrolyte. *Phys. Chem. Chem. Phys.* **2016**, *18* (32), 22540–22547.
- (43) Choi, Y. S.; Lee, Y. S.; Choi, D. J.; Chae, K. H.; Oh, K. H.; Cho, Y. W. Enhanced Li ion conductivity in LiBH_4 - Al_2O_3 mixture via interface engineering. *J. Phys. Chem. C* **2017**, *121* (47), 26209–26215.
- (44) Gutowska, A.; Li, L. Y.; Shin, Y. S.; Wang, C. M. M.; Li, X. H. S.; Linehan, J. C.; Smith, R. S.; Kay, B. D.; Schmid, B.; Shaw, W.; et al. Nanoscaffold mediates hydrogen release and the reactivity of ammonia borane. *Angew. Chem., Int. Ed.* **2005**, *44* (23), 3578–3582.
- (45) Berube, V.; Radtke, G.; Dresselhaus, M.; Chen, G. Size effects on the hydrogen storage properties of nanostructured metal hydrides: A review. *Int. J. Energy Res.* **2007**, *31* (6–7), 637–663.
- (46) de Jongh, P. E.; Adelhelm, P. Nanosizing and nanoconfinement: new strategies towards meeting hydrogen storage goals. *ChemSusChem* **2010**, *3* (12), 1332–1348.
- (47) Ngene, P.; van Zwienen, M.; de Jongh, P. E. Reversibility of the hydrogen desorption from LiBH_4 : a synergetic effect of nanoconfinement and Ni addition. *Chem. Commun.* **2009**, *46* (43), 8201–8203.
- (48) Suwarno; Ngene, P.; Nale, A.; Eggenhuisen, T. M.; Oschatz, M.; Embs, J. P.; Remhof, A.; de Jongh, P. E. Confinement effects for lithium borohydride: comparing silica and carbon scaffolds. *J. Phys. Chem. C* **2017**, *121* (8), 4197–4205.
- (49) Maier, J. Ionic-conduction in space charge regions. *Prog. Solid State Chem.* **1995**, *23* (3), 171–263.
- (50) Verdal, N.; Udovic, T. J.; Rush, J. J.; Liu, X. F.; Majzoub, E. H.; Vajo, J. J.; Gross, A. F. Dynamical perturbations of tetrahydroborate anions in LiBH_4 due to nanoconfinement in controlled-pore carbon scaffolds. *J. Phys. Chem. C* **2013**, *117* (35), 17983–17995.
- (51) Breuer, S.; Uitz, M.; Wilkening, H. M. R. Rapid Li ion dynamics in the interfacial regions of nanocrystalline solids. *J. Phys. Chem. Lett.* **2018**, *9* (8), 2093–2097.
- (52) de Jongh, P. E.; Eggenhuisen, T. M. Melt infiltration: an emerging technique for the preparation of novel functional nanostructured materials. *Adv. Mater.* **2013**, *25* (46), 6672–6690.
- (53) Unemoto, A.; Yasaku, S.; Nogami, G.; Tazawa, M.; Taniguchi, M.; Matsuo, M.; Ikeshoji, T.; Orimo, S. Development of bulk-type all-solid-state lithium-sulfur battery using LiBH_4 electrolyte. *Appl. Phys. Lett.* **2014**, *105* (8), 083901.
- (54) Das, S.; Ngene, P.; Norby, P.; Vegge, T.; de Jongh, P. E.; Blanchard, D. All-solid-state lithium-sulfur battery based on a nanoconfined LiBH_4 electrolyte. *J. Electrochem. Soc.* **2016**, *163* (9), A2029–A2034.
- (55) Lefevr, J.; Cervini, L.; Griffin, J. M.; Blanchard, D. Lithium conductivity and ions dynamics in $\text{LiBH}_4/\text{SiO}_2$ solid electrolytes studied by solid-state NMR and quasi-elastic neutron scattering and applied in lithium sulfur batteries. *J. Phys. Chem. C* **2018**, *122* (27), 15264–15275.
- (56) Cheng, C.-F.; Zhou, W.; Ho Park, D.; Klinowski, J.; Hargreaves, M.; Gladden, L. F. Controlling the channel diameter of the

mesoporous molecular sieve MCM-41. *J. Chem. Soc., Faraday Trans.* **1997**, 93 (2), 359–363.

(57) Zhao, D. Y.; Feng, J. L.; Huo, Q. S.; Melosh, N.; Fredrickson, G. H.; Chmelka, B. F.; Stucky, G. D. Triblock copolymer syntheses of mesoporous silica with periodic 50 to 300 angstrom pores. *Science* **1998**, 279 (5350), 548–552.

(58) Hartman, M. R.; Rush, J. J.; Udovic, T. J.; Bowman, R. C.; Hwang, S. J. Structure and vibrational dynamics of isotopically labeled lithium borohydride using neutron diffraction and spectroscopy. *J. Solid State Chem.* **2007**, 180 (4), 1298–1305.

(59) Filinchuk, Y.; Chernyshov, D.; Cerny, R. Lightest borohydride probed by synchrotron X-ray diffraction: Experiment calls for a new theoretical revision. *J. Phys. Chem. C* **2008**, 112 (28), 10579–10584.

(60) Hanawalt, J. D.; Rinn, H. W.; Frevel, L. K. Chemical analysis by X-ray diffraction - Classification and use of X-ray diffraction patterns. *Ind. Eng. Chem., Anal. Ed.* **1938**, 10, 0457–0512.

(61) Posnjak, E. W. R. Crystal structure of alkali halogenides. *J. Wash. Acad. Sci.* **1922**, 12, 248–251.

(62) Royer, L. Sur les accolements reguliers de cristaux d'especes differentes. *C. R. Hebd. Seances Acad. Sci.* **1925**, 180, 2050.

(63) Harvey, K. B.; Mcquaker, N. R. Low temperature infrared and raman spectra of lithium borohydride. *Can. J. Chem.* **1971**, 49 (20), 3282.

(64) D'Anna, V.; Spyratou, A.; Sharma, M.; Hagemann, H. FT-IR spectra of inorganic borohydrides. *Spectrochim. Acta, Part A* **2014**, 128, 902–906.

(65) D'Anna, V.; Daku, L. M. L.; Hagemann, H. Quantitative spectra-structure relations for borohydrides. *J. Phys. Chem. C* **2015**, 119 (38), 21868–21874.

(66) Coates, J. Interpretation of infrared spectra, a practical approach. *Encycl. Anal. Chem.* **2006**, 1, 10815–10837.

(67) Sun, T.; Liu, J.; Jia, Y.; Wang, H.; Sun, D. L.; Zhu, M.; Yao, X. D. Confined LiBH_4 : Enabling fast hydrogen release at similar to 100 degrees C. *Int. J. Hydrogen Energy* **2012**, 37 (24), 18920–18926.

(68) Plerdsranoy, P.; Utke, R. Confined LiBH_4 - LiAlH_4 in nanopores of activated carbon nanofibers. *Int. J. Hydrogen Energy* **2015**, 40 (22), 7083–7092.

(69) Javadian, P.; Sheppard, D. A.; Buckley, C. E.; Jensen, T. R. Hydrogen storage properties of nanoconfined LiBH_4 - NaBH_4 . *Int. J. Hydrogen Energy* **2015**, 40 (43), 14916–14924.

(70) Laiti, E.; Persson, P.; Ohman, L. O. Balance between surface complexation and surface phase transformation at the alumina/water interface. *Langmuir* **1998**, 14 (4), 825–831.

(71) Hiyoshi, N.; Yogo, K.; Yashima, T. Adsorption characteristics of carbon dioxide on organically functionalized SBA-15. *Microporous Mesoporous Mater.* **2005**, 84 (1–3), 357–365.

(72) Zhao, X. S.; Lu, G. Q. Modification of MCM-41 by surface silylation with trimethylchlorosilane and adsorption study. *J. Phys. Chem. B* **1998**, 102 (9), 1556–1561.

(73) Irvine, J. T. S.; Sinclair, D. C.; West, A. R. Electroceramics: Characterization by impedance spectroscopy. *Adv. Mater.* **1990**, 2, 132–138.

(74) Verkuijlen, M. H. W.; Ngene, P.; de Kort, D. W.; Barre, C.; Nale, A.; van Eck, E. R. H.; van Bentum, P. J. M.; de Jongh, P. E.; Kentgens, A. P. M. Nanoconfined LiBH_4 and enhanced mobility of Li^+ and BH_4^- studied by solid-state NMR. *J. Phys. Chem. C* **2012**, 116 (42), 22169–22178.

(75) Epp, V.; Wilkening, M. Fast Li diffusion in crystalline LiBH_4 due to reduced dimensionality: Frequency-dependent NMR spectroscopy. *Phys. Rev. B: Condens. Matter Mater. Phys.* **2010**, 82 (2), 020301.